

Determining 3D atomic coordinates of light-element quantum materials using ptychographic electron tomography

Na Yeon Kim^{1*}, Hanfeng Zhong^{1,2*}, Jianhua Zhang^{3*}, Colum M. O’Leary^{1*}, Yuxuan Liao¹, Ji Zou⁴, Haozhi Sha¹, Minh Pham¹, Weiyi Li¹, Yakun Yuan¹, Ji-Hoon Park⁵, Dennis Kim⁶, Huaidong Jiang³, Jing Kong⁵, Miaofang Chi⁷, Jianwei Miao^{1†}

¹Department of Physics and Astronomy and California NanoSystems Institute, University of California, Los Angeles, CA, USA.

²Department of Electrical and Computer Engineering, University of California, Los Angeles, CA, USA.

³Center for Transformative Science, ShanghaiTech University, Shanghai, China. ⁴Department of Physics, University of Basel, Basel, Switzerland.

⁵Department of Electrical Engineering and Computer Science, Massachusetts Institute of Technology, Cambridge, MA, USA.

⁶Department of Chemistry and Biochemistry, University of California, Los Angeles, CA, USA.

⁷Center for Nanophase Materials Sciences, Oak Ridge National Laboratory, Oak Ridge, TN, USA.

*These authors contributed equally to this work. †Correspondence author. Email:

j.miao@ucla.edu

Understanding quantum materials at the atomic scale requires precise 3D characterization of atomic positions and crystal defects. However, resolving the 3D structure of light-element materials ($Z \leq 8$) remains a major challenge due to their low contrast and beam damage in electron microscopy. Here, we demonstrate ptychographic atomic electron tomography (pAET), achieving sub-ångström 3D atomic precision (0.11

Å) in light elements, marking the first-ever experimental realization of 3D atomic imaging for light-element materials. Using twisted bilayer graphene as a model system, we determine the 3D atomic coordinates of individual carbon atoms, revealing chiral lattice distortions driven by van der Waals interactions that exhibit meron-like and skyrmion-like structures. These findings provide direct insights into the interplay between 3D chiral lattice deformation and electronic properties in moiré materials. Beyond TBG, pAET offers a transformative approach for 3D atomic-scale imaging across quantum materials, 2D heterostructures, functional oxides, and energy materials.

Atomic-scale structural characterization is crucial for understanding quantum materials (1), where phenomena such as topological insulators (2, 3), single-photon emitters (4), and unconventional superconductors (5, 6) emerge from local atomic configurations. Traditional imaging methods, including scanning probe microscopy (5, 7, 8), transmission electron microscopy (9-12), and scanning transmission electron microscopy (STEM) (13-16), primarily provide surface-sensitive or 2D structural information, limiting insights into 3D atomic arrangements. While atomic electron tomography (AET) based on STEM has achieved 3D atomic imaging for heavy-element materials ($Z \geq 16$) without requiring crystallinity (17-22), current methods fail to resolve the 3D atomic positions and crystal defects in light-element quantum materials ($Z \leq 8$) due to low contrast and electron beam damage from high-energy (≥ 80 keV) electrons (23). Here, we demonstrate that ptychographic AET (pAET) overcomes these limitations, enabling high-precision 3D atomic structure determination of light-element quantum materials. By integrating ptychographic phase retrieval with AET, pAET achieves 3D imaging of individual carbon atoms with 11 pm precision, surpassing conventional imaging techniques.

Ptychographic electron tomography experiment of TBG

To illustrate the capabilities of pAET, we selected twisted bilayer graphene (TBG) as a model system due to its significance as a quantum material (24) and the necessity to resolve 3D atomic positions for deeper insight into interlayer interactions within moiré patterns (25). The TBG sample was prepared by stacking graphene monolayers at a small twist angle (26). A focused electron probe was used for single-atom fabrication, introducing individual silicon dopants at defect sites in TBG (fig. S1) (26). These dopants induced local strain and served as reference points for tomographic alignment (17). The experiment was conducted using a Nion microscope, where the TBG sample was tilted to 13 different angles using a double-tilt stage. At each tilt angle, diffraction patterns were acquired by scanning the sample with a 70 keV electron probe in a 2D raster scan (Fig. 1A and table S1). These diffraction patterns encode electron-sample interactions, providing input for computational phase retrieval algorithms that reconstruct the complex functions of both the sample and the probe (22). By capturing nearly all transmitted and diffracted electrons, ptychography enhances the signal-to-noise ratio and spatial resolution, overcoming the limitations of conventional electron microscopy (27).

Reconstruction was performed using the multimode extended ptychographic iterative engine (ePIE) (28), incorporating four orthogonal probe modes to account for partial coherence and measurement imperfections (fig. S2) (29). The reconstructed phase images of TBG at 13 tilt angles are shown in fig. S3 and movie S1, with individual silicon dopants visible. High-precision tomographic reconstruction required accurate tilt angle calibration, which was achieved using nanoparticles as fiducial markers in low-magnification annular dark-field images (fig. S4), acquired simultaneously during the ptychography experiment. The calibrated angles were refined and combined with silicon dopants to align the 13 ptychographic projections (26). To ensure consistency, the phase images were scaled to maintain a uniform mean phase value across all projections.

Precisely resolving 3D atomic positions in TBG

Following image pre-processing, the 13 ptychographic projections and their calibrated angles were used to reconstruct the 3D atomic structure of TBG (26). To mitigate the limited tilt range constraint of the Nion microscope, we developed two key strategies to enhance the precision of pAET. First, we incorporated a 3D electron probe into the tomographic reconstruction to correct for tilt-dependent defocus gradients across the sample (26). Second, we applied a 1D support constraint using a generalized Gaussian distribution, ensuring robustness and accuracy in 3D atomic reconstruction. Tomographic reconstruction was performed using the real-space iterative reconstruction algorithm, which monitored convergence via an error function and enabled automated refinement of positions and angles (26, 30). In each iteration, the 3D object was deconvolved from the electron probe, resulting in sharper atomic peaks and reduced spatial overlap along the depth (z) axis (Fig. 1B). The projected profile of the 3D reconstruction along the z-axis reveals two distinct peaks, corresponding to two graphene layers. The slight asymmetry between these peaks arises from structural disorder in TBG. Using this two-peak profile, we defined a loose 1D support along the z-axis with a generalized Gaussian distribution and applied it iteratively to the 3D structure at each reconstruction step. By varying the kernel size of the generalized Gaussian function, we achieved consistent 3D reconstructions, demonstrating the robustness and reproducibility of this method (Fig. 1, C and D). Figure 1, E and F, displays the top and bottom layers of TBG, clearly showing layer separation after applying the 3D electron probe and 1D support constraint (Fig. 1G).

To improve atomic precision given the limited number of tilt angles and the presence of a large missing wedge, we developed an iterative atom-tracing method to extract 3D atomic coordinates from the experimental tomographic reconstruction (26). Unlike previous non-iterative atom-tracing approaches (18-21), this method iteratively refines atomic positions, with tracing errors converging after just a few iterations (fig. S5). The traced 3D atomic positions

were then refined using gradient descent, which minimized the error between the calculated and experimental projections. Each atom was represented as a 3D Gaussian function, incorporating electron probe size and thermal motion effects. Projections were generated using the experimental tilt angles, and to further improve precision, both atomic positions and tilt angles were optimized. For each experimental projection, a series of calculated projections was generated across a range of tilt angles centered around calibrated values. The tilt angles were iteratively optimized by comparing the calculated and experimental projections, ensuring accurate atomic reconstruction. This iterative refinement process continued until no further improvement was observed, yielding the final 3D experimental atomic model of TBG (Fig. 1A, and movie S1).

To assess the 3D precision of pAET, we performed multislice simulations to generate 13 sets of ptychographic diffraction patterns from the experimental 3D atomic model and refined tilt angles, under identical experimental conditions (table S1) (26). To accurately model thermal vibrations of atoms, we incorporated 64 frozen phonons into the multislice simulations. Poisson noise was added to the diffraction patterns to simulate realistic conditions, and 13 ptychographic phase images were reconstructed using the multimode ePIE algorithm (28, 29). To account for broadening effects caused by electron probe interactions and sample drift, we applied Gaussian convolution to each image. The kernel size was optimized to minimize discrepancies between the multislice and experimental phase images. Using the 13 multislice phase images, we applied the same pAET procedures as for experimental data to reconstruct and refine a new 3D atomic model. Figure 2, A-C, displays histograms of deviations between the experimental and refined 3D atomic models along the x, y, and z axes, showing root mean square deviations (RMSD) of 5, 6, and 7 pm, respectively. The overall RMSD between the two models is 11 pm (Fig. 2D), marking a significant advancement over previous pAET results in both precision and capability to resolve individual light atoms (31–34).

Using the experimental 3D atomic model, we determined the twist angle of TBG to be 1.97° , and identified the 3D coordinates of 6,649 carbon atoms and 3 silicon atoms. Figure 2, E and F, shows the top and bottom layers of the experimental atomic model. The average interlayer distance was measured as 3.43 \AA (fig. S6). The yellow and blue regions indicate upward and downward curvature within the layers, while black lines illustrate sp^2 C-C bonds. Figure 2G presents a histogram of bond lengths, revealing a mean of 1.44 \AA with a standard deviation of 0.02 \AA . This closely aligns with the 1.425 \AA bond length predicted by the density functional theory (DFT)-relaxed atomic model (fig. S7B). Each layer exhibits atomic corrugations along the z-axis within a $\pm 0.1 \text{ \AA}$ range, influenced by stacking configurations, strain, and silicon dopants.

A particularly noteworthy feature is that atomic corrugations in the experimental model exhibit significantly greater intricacy than those predicted by the DFT-relaxed model (figs. S6 and S7). Notably, we observed distinct behaviors in the AA stacking regions: in one region (AA1, Fig. 2, E and F), the two graphene layers curve upward, while in the other (AA2, Fig. 2, E and F), the layers display a bulging deformation. These intricate atomic corrugations can induce charge redistribution, disrupt rotational symmetry, and modify the electronic band structure of TBG (35). Precise experimental measurements enabled a detailed quantitative analysis of interlayer distance variations as a function of local stacking configurations. The interlayer distance was determined to be $3.45 \pm 0.02 \text{ \AA}$ in the AA regions and $3.41 \pm 0.03 \text{ \AA}$ in the AB/BA regions (Fig. 2H). These values exhibit larger variability than those predicted by the DFT-relaxed model (fig. S7C), highlighting the intricate complexity of atomic corrugations in real TBG.

Quantifying 3D chiral lattice distortions in TBG

Accurately measuring atomic coordinates in TBG enabled us to quantitatively analyze the 3D displacement vector field, marking a significant advancement over previous studies that were limited to 2D experimental methods (36, 37). To investigate the 3D displacement field induced by van der Waals interactions, we compared the experimental 3D atomic model with an unrelaxed TBG model consisting of two flat graphene layers (26). This comparison allowed us to extract 3D displacement vectors for both the top and bottom layers of TBG (Fig. 2, A and B). The displacement vectors exhibit high vorticity within the xy-plane around the AA stacking regions, accompanied by an out-of-plane z component, indicating the presence of chiral lattice distortions. These displacement field textures closely resemble magnetic merons and skyrmions (38).

To quantify this behavior, we calculated the solid angle subtended by each configuration, known as the skyrmion number (N_s) (26). The experimental TBG model reveals two meron-like, three anti-meron-like, and one anti-skyrmion-like structure. Figure 3, A and B, illustrates the 3D vector textures of a meron-like and an anti-meron-like structure, both exhibiting elliptical shapes with N_s values of -0.42 and 0.46, respectively. Additional meron-like and anti-meron-like structures are presented in fig. S8, A-C. The displacement vectors align with the z-axis near the core, gradually increasing their polar angle toward the boundary and predominantly tilting into the xy-plane at the boundary. These experimental vector textures deviate from the relaxed TBG model, which exhibits perfectly symmetrical meron-like and anti-meron-like structures (fig. S9, A and B) with N_s values of -0.5 and +0.5, respectively. Figure 3C depicts the 3D vector texture of an anti-skyrmion-like structure, which has an elliptical shape and an N_s value of 0.97. The anti-skyrmion-like structure features an anti-meron-like core (Fig. 3B), with some boundary vectors tilting their polar angle to nearly 180° . Compared to its counterpart in the relaxed TBG model (fig. S9C), the experimental anti-

skyrmion-like structure exhibits more pronounced distortions in shape, skyrmion number, and 3D vector texture.

To investigate how chiral lattice distortions affect the electronic structure of TBG, we integrated experimentally measured 3D atomic coordinates into DFT calculations. While DFT has been widely used to predict TBG's electronic properties (39), it typically introduces defects into ideal lattices and relaxes atomic configurations to their ground states. By incorporating experimental 3D atomic coordinates directly into DFT, we derived a more accurate electronic band structure for TBG. Figure 4A presents a moiré supercell containing 3,267 carbon atoms and a silicon dopant, including two anti-meron-like structures. The experimental 3D atomic coordinates exhibit greater variations along the z-axis than the relaxed model (Fig. 4, B and C). These coordinates were directly integrated into DFT to obtain the band structures. Figure 4D compares the electronic band structure derived from the experimental 3D coordinates with that of the relaxed model. In the relaxed model, the valence and conduction bands converge at the K point at the Fermi level (green). The presence of a zero-bandgap Dirac cone suggests that relaxed TBG behaves as a semimetal, similar to single-layer graphene (40).

In contrast, the experimental moiré supercell exhibits a Dirac cone with a 22 meV bandgap (blue). At room temperature, the thermal energy (26 meV) is sufficient to excite charge carriers across this bandgap. As the temperature decreases, the number of thermally excited carriers declines exponentially, lowering the carrier concentration and making TBG increasingly insulating at lower temperatures. Additionally, the larger z-axis atomic displacements in the experimental model increase the valence band energy while lowering the conduction band energy at the Γ point. This results in a bandwidth reduction at the Γ point by up to 13.5%, suggesting stronger electron interactions between the top and bottom layers of real TBG.

Conclusions and Outlook

Quantum materials exhibit unique physical properties driven by strong local order or disorder at the atomic scale (1–6). However, directly resolving their 3D atomic structures remains challenging due to the prevalence of light elements, which pose limitations in conventional imaging techniques. In this work, we demonstrate pAET as a breakthrough approach, achieving sub-ångström precision in determining the 3D coordinates of individual carbon atoms in TBG with an accuracy of 11 pm. Our findings reveal interlayer spacing variations across TBG, with their magnitude strongly influenced by local stacking configurations. By quantifying the 3D displacement vector field, we provide the first experimental evidence of 3D chiral lattice distortions induced by van der Waals interactions, uncovering meron-like, anti-meron-like, and anti-skyrmion-like structures. Additionally, integrating our experimentally measured 3D atomic coordinates into DFT calculations reveals an asymmetric band structure with a 22 meV bandgap, whereas the relaxed atomic structure exhibits a zero-bandgap Dirac cone.

While TBG serves as a proof of principle, our multislice simulations suggest that pAET is capable of resolving nitrogen-vacancy color centers and their 3D local environments within a 15-nm-thick diamond nanocrystal using a 70 keV electron probe (fig. S10). These results underscore the transformative potential of pAET in bridging the gap between structural characterization and quantum phenomena. Beyond TBG, we anticipate that pAET will revolutionize atomic-scale imaging across a broad range of quantum and functional materials, facilitating direct correlations between crystal defects, structural disorder, and material properties. This technique is expected to impact van der Waals heterostructures (25), quantum emitters (4, 41), topological insulators (2, 3), superconductors (5, 6, 42), charge-density waves (43), ferroelectrics (44, 45), and catalysts (46), offering unprecedented insight into their 3D atomic architectures and emergent quantum behaviors.

REFERENCES

1. D. N. Basov, R. D. Averitt, D. Hsieh, *Nat. Mater.* **16**, 1077–1088 (2017).
2. L. A. Wray *et al.*, *Nat. Phys.* **7**, 32-37 (2011).
3. C. W. Peterson, T. Li, W. Jiang, T. L. Hughes, G. Bahl, *Nature* **589**, 376-380 (2021).
4. I. Aharonovich, D. Englund, M. Toth, *Nat. Photon.* **10**, 631-641 (2016).
5. M. Oh *et al.*, *Nature* **600**, 240-245 (2021).
6. S. H. Pan *et al.*, *Nature* **403**, 746-750 (2000).
7. Y. Jiang *et al.*, *Nature* **573**, 91-95 (2019).
8. L. J. McGilly *et al.*, *Nat. Nanotechnol.* **15**, 580-584 (2020).
9. C. Gómez-Navarro *et al.*, *Nano Lett.* **10**, 1144-1148 (2010).
10. J. C. Meyer *et al.*, *Nat. Mater.* **10**, 209-215 (2011).
11. J. H. Warner *et al.*, *Science* **337**, 209-212 (2012).
12. H. Yoo *et al.*, *Nat. Mater.* **18**, 448-453 (2019).
13. O. L. Krivanek *et al.*, *Nature* **464**, 571-574 (2010).
14. W. Zhou *et al.*, *Nano Lett.* **13**, 2615-2622 (2013).
15. Y.-C. Lin, D. O. Dumcenco, Y.-S. Huang, K. Suenaga, *Nat. Nanotechnol.* **9**, 391-396 (2014).
16. A. Weston *et al.*, *Nat. Nanotechnol.* **15**, 592–597 (2020).
17. J. Miao, P. Ercius, S. J. Billinge, *Science* **353**, aaf2157 (2016).
18. Y. Yang *et al.*, *Nature* **542**, 75-79 (2017).
19. X. Tian *et al.*, *Nat. Mater.* **19**, 867-873 (2020).
20. Y. Yang *et al.*, *Nature* **592**, 60-64 (2021).
21. X. Tian *et al.*, *Sci. Adv.* **7**, eabi6699 (2021).
22. J. Miao, *Nature* **637**, 281–295 (2025).
23. R. F. Egerton, *Ultramicroscopy* **145**, 85-93 (2014).

24. E. Y. Andrei, A. H. MacDonald, *Nat. Mater.* **19**, 1265-1275 (2020).
25. K. S. Novoselov, A. Mishchenko, A. Carvalho, A. H. Castro Neto, *Science* **353**, aac9439 (2016).
26. Materials, methods and supplementary text are available as supplementary materials.
27. Y. Jiang *et al.*, *Nature* **559**, 343–349 (2018).
28. A. M. Maiden, J. M. Rodenburg, *Ultramicroscopy* **109**, 1256-1262 (2009).
29. Z. Chen *et al.*, *Nat. Commun.* **11**, 2994 (2020).
30. M. Pham, Y. Yuan, A. Rana, S. Osher, J. Miao, *Sci. Rep.* **13**, 5624 (2023).
31. D. J. Chang *et al.*, *Phys. Rev. B* **102**, 174101 (2020).
32. P. M. Pelz *et al.*, *Nat. Commun.* **14**, 7906 (2023).
33. J. Lee, M. Lee, Y. Park, C. Ophus, Y. Yang, *Phys. Rev. Applied* **19**, 054062 (2023).
34. A. Romanov, M. G. Cho, M. C. Scott, P. M. Pelz, *J. Phys. Mater.* **8**, 015005 (2025).
35. T. Ohta, A. Bostwick, T. Seyller, K. Horn, E. Rotenberg, *Science* **313**, 951-954 (2006).
36. N. P. Kazmierczak *et al.*, *Nat. Mater.* **20**, 956–963 (2021).
37. S. H. Sung *et al.*, *Nat. Commun.* **13**, 7826 (2022).
38. X. Z. Yu *et al.*, *Nature* **564**, 95–98 (2018).
39. S. Carr, S. Fang, E. Kaxiras, *Nat. Rev. Mater.* **5**, 748–763 (2020).
40. A. H. Castro Neto, N. M. R. Peres, K. S. Novoselov, A. K. Geim, *Rev. Mod. Phys.* **81**, 109-162 (2009).
41. X. Liu, M. C. Hersam, *Nat. Rev. Mater.* **4**, 669-684 (2019).
42. Z. Dong *et al.*, *Nature* **630**, 847–852 (2024).
43. G. Grüner, *Rev. Mod. Phys.* **60**, 1129-1181 (1988).
44. J. F. Scott, *Science* **315**, 954-959 (2007).
45. M. E. Lines, A. M. Glass, *Principles and Applications of Ferroelectrics and Related Materials* (Oxford Univ. Press, 2001).

46. Y. Yang *et al.*, *Nat. Catal.* **7**, 796-806 (2024).

ACKNOWLEDGMENTS

Funding: We gratefully acknowledge Juan Carlos Idrobo and Andrew R. Lupini for their assistance with the experiments, and Yao Yang for help with data analysis. This research was primarily supported by the U.S. Department of Energy, Office of Science, Basic Energy Sciences, Division of Materials Sciences and Engineering, under award no. DE-SC0010378. N.Y.K., C.O.L., J.M., J.-H.P., and J.K. acknowledge support from the U.S. Army Research Office (ARO) MURI project under grant W911NF-18-1-04320431 acknowledge the support from the U.S. Army Research Office (ARO) MURI project under grant W911NF-18-1-04320431. J.Z. acknowledges the support from the Georg H. Endress Foundation. The electron ptychography and STEM imaging experiments were carried out at the Center for Nanophase Materials Sciences (CNMS), Oak Ridge National Laboratory (ORNL). **Author contributions:** J.M. directed the project. J.H.P. and J.K. synthesized the graphene samples. N.Y.K., C.M.O., M.C. and J.M. discussed and/or conducted the experiments. J. Zhang, H.S., C.M.O., H.Z., N.Y.K., H.J. and J.M. contributed to the discussions and/or performed the ptychographic reconstructions. Y.Y., Y.L., M.P., H.Z. and J.M. developed and implemented the 3D electron probe into the tomographic reconstruction framework. H.Z., N.Y.K., C.M.O., Y.L., J. Zou, H.S., W.L., Y.Y., D.K. and J.M. carried out the tomographic reconstructions, atom tracing, classification, data analysis, and/or result interpretation. N.Y.K., C.M.O., H.Z., Y.L. and J.M. wrote the manuscript. All authors commented on the manuscript. **Competing interests:** The authors declare no competing interests. **Data and materials availability:** All raw and processed experimental data, along with MATLAB source codes for ptychographic and tomographic reconstructions, atom tracing and refinement, and data analysis from this work will be promptly posted on GitHub upon publication.

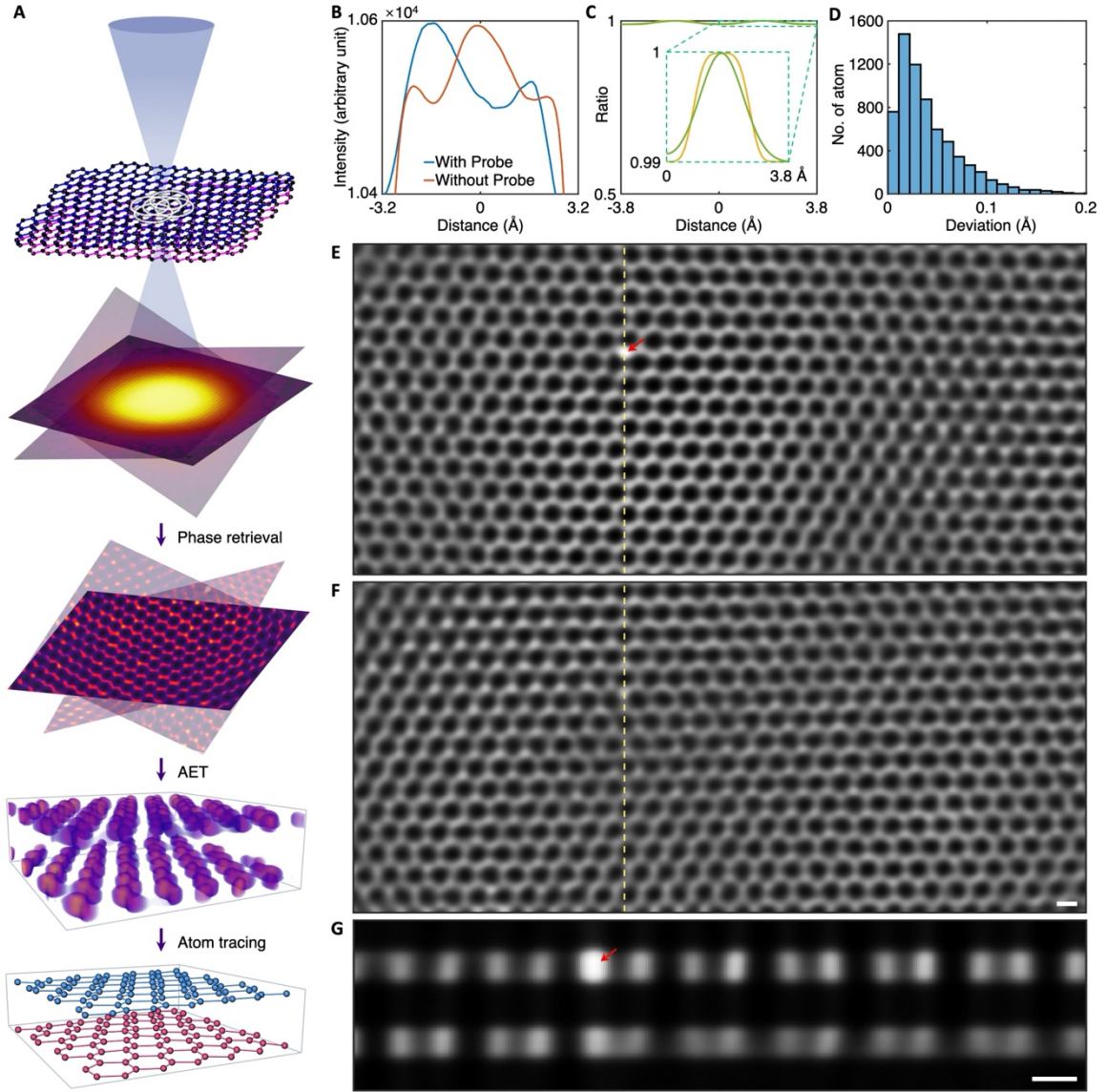


Fig. 1. Experimental demonstration of pAET for resolving the 3D coordinates of individual carbon atoms. (A) Schematic of pAET applied to TBG. A focused electron probe scans the sample, generating an array of diffraction patterns, which are subsequently processed to reconstruct phase images. These phase images serve as input for tomographic reconstruction, enabling precise atomic position tracing and refinement. (B) Integration of the 3D electron probe into tomographic reconstruction enhances layer separation in TBG, improving depth resolution. (C) Application of a 1D support constraint along the z-axis, modeled using a generalized Gaussian distribution with varying kernel sizes (yellow and green). This constraint

is iteratively applied during tomographic reconstruction to improve structural accuracy. **(D)** Comparison of tomographic reconstructions using different kernel sizes, demonstrating the effect of kernel variation on reconstruction accuracy. An RMSD of 5 pm is achieved, highlighting the high precision of pAET. **(E, F)** Differentiation of the top **(E)** and bottom **(F)** graphene layers after incorporating both the 3D electron probe and the 1D support constraint. Red arrows indicate silicon dopants. **(G)** Projected view of the two graphene layers along the z-axis, highlighting the region marked by yellow lines in **(E)** and **(F)**, confirming successful layer separation. Scale bars, 2 Å.

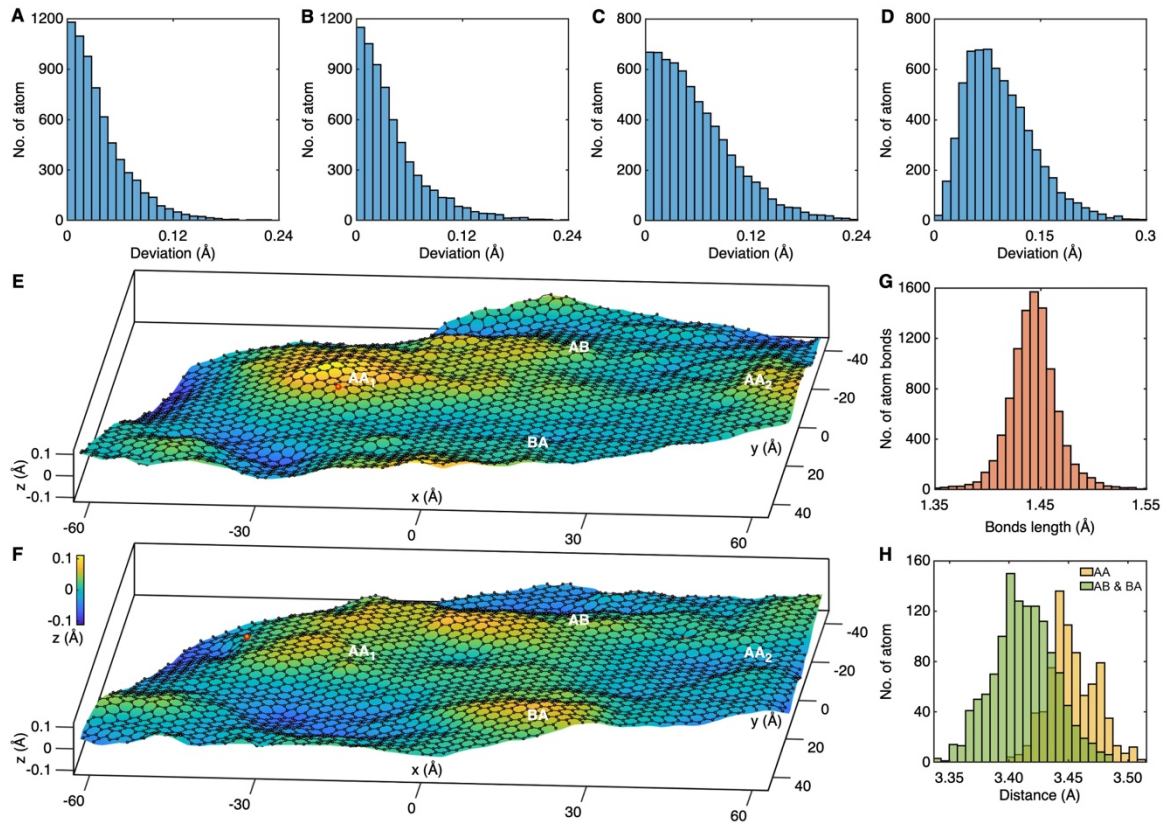


Fig. 2. 3D atomic corrugations in TBG induced by interatomic interactions. (A-C) Histograms of 3D atomic position deviations between the experimental and multislice simulation models along the x, y, and z axes, with RMSDs of 5 pm, 6 pm, and 7 pm, respectively. **(D)** Histogram of the overall 3D atomic position deviations between the two models, yielding an RMSD of 11 pm, demonstrating high reconstruction precision. **(E, F)** Top and bottom layers

of the experimental atomic model, where yellow regions indicate upward curvature, and blue regions indicate downward curvature within the layers. To enhance precision while balancing resolution, atomic positions were smoothed using a 3D Gaussian kernel, with half the lattice constant applied along the x- and y-axes ($\sigma_x = \sigma_y = 1.26 \text{ \AA}$) and half the average interlayer distance along the z-axis ($\sigma_z = 1.71 \text{ \AA}$). (G) Histogram of sp^2 C–C bond lengths, with a mean of 1.44 \AA . (H) Histogram of interlayer distances in the AA and AB/BA stacking regions, revealing mean values of 3.45 \AA and 3.41 \AA , respectively, highlighting subtle interlayer variations.

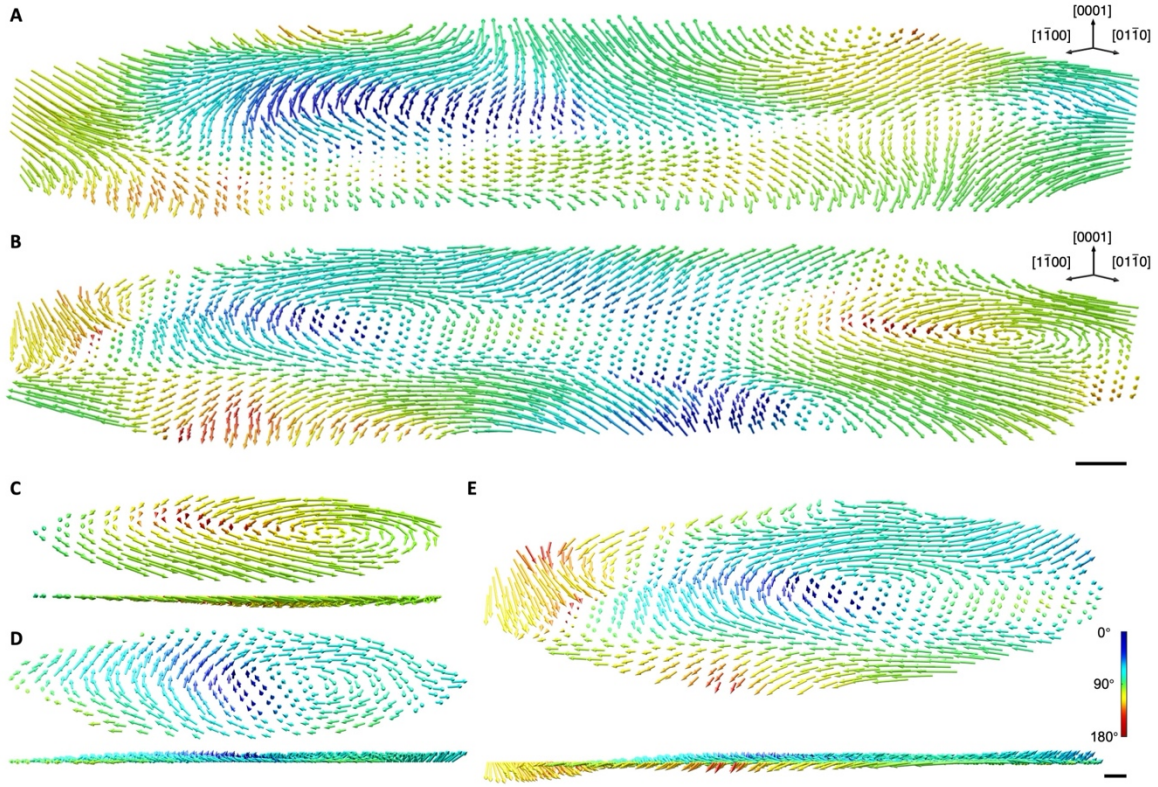


Fig. 3. Quantifying 3D displacement vectors and chiral lattice distortions in TBG. (A, B) Experimental 3D displacement vectors in the top and bottom layers of TBG, with vector colors representing the polar angle relative to the xy-plane. (C, D) 3D vector textures of a meron-like structure (C) and an anti-meron-like structure (D). Near the core, vectors align along the z-axis and gradually tilt into the xy-plane toward the boundary as their polar angles increase,

indicating chiral lattice distortions. (E) 3D vector field of an anti-skyrmion-like structure, featuring an anti-meron-like core (D). Some boundary vectors exhibit polar angles approaching 180° , demonstrating complex topological distortions. To enhance visual clarity, vector magnitudes are amplified by a factor of 25. Scale bar, 5 Å in (B) and 2 Å in (E).

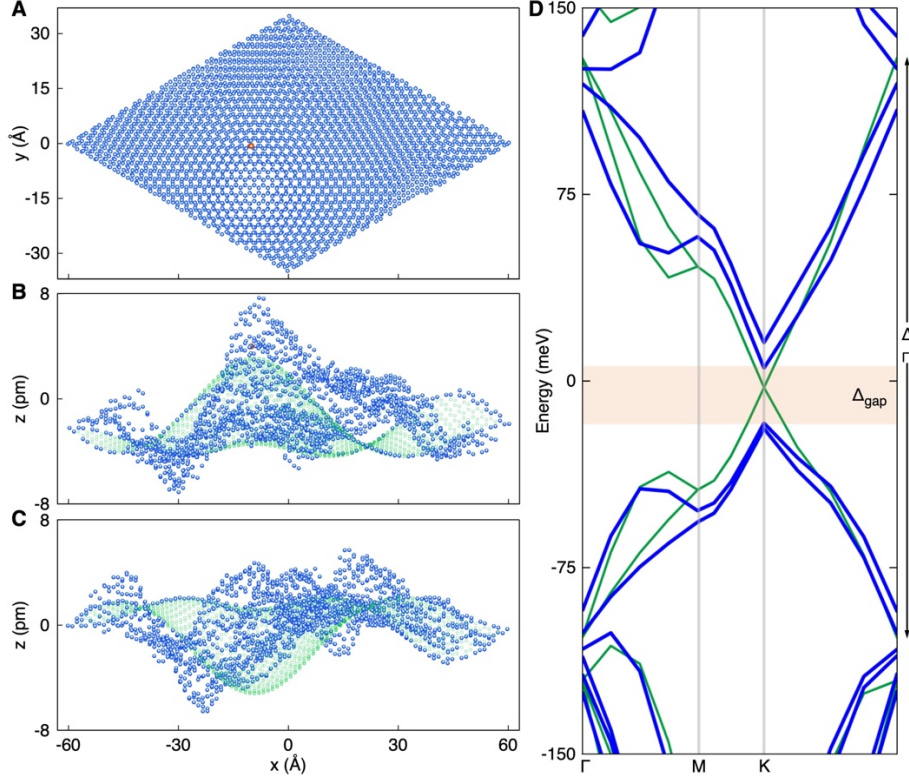


Fig. 4. Comparison of TBG's electronic band structures between experimental and DFT-relaxed atomic models. (A) Experimental 3D atomic model of a moiré supercell, containing 3,267 carbon atoms and one silicon dopant (red dot), featuring two anti-meron-like structures. (B, C) Comparison of experimental (blue) and DFT-relaxed (green) atomic positions in the top (B) and bottom (C) graphene layers. The experimental model exhibits greater z-axis variations, indicating structural corrugation that deviates from the relaxed configuration. (D) Electronic band structure comparison between the experimental and DFT-relaxed models. The experimental model (blue) reveals an asymmetric band structure, with a 22 meV bandgap at the K point and up to a 13.5% bandwidth reduction at the Γ point, whereas the DFT-relaxed model (green) maintains a symmetric band structure with a Dirac cone.